

# Raman Lidar Profiling of Atmospheric Water Vapor: Simultaneous Measurements with Two Collocated Systems

J. E. M. Goldsmith,\*  
Scott E. Bisson,\*  
Richard A. Ferrare,†  
Keith D. Evans,†  
David N. Whiteman,\*\*  
and S. H. Melfi\*\*

## Abstract

Raman lidar is a leading candidate for providing the detailed space- and time-resolved measurements of water vapor needed by a variety of atmospheric studies. Simultaneous measurements of atmospheric water vapor are described using two collocated Raman lidar systems. These lidar systems, developed at the NASA/Goddard Space Flight Center and Sandia National Laboratories, acquired approximately 12 hours of simultaneous water vapor data during three nights in November 1992 while the systems were collocated at the Goddard Space Flight Center. Although these lidar systems differ substantially in their design, measured water vapor profiles agreed within  $0.15 \text{ g kg}^{-1}$  between altitudes of 1 and 5 km. Comparisons with coincident radiosondes showed all instruments agreed within  $0.2 \text{ g kg}^{-1}$  in this same altitude range. Both lidars also clearly showed the advection of water vapor in the middle troposphere and the pronounced increase in water vapor in the nocturnal boundary layer that occurred during one night.

## 1. Introduction

Detailed measurements of the distribution of water vapor in the atmosphere are needed for a variety of scientific inquiries, including global climate change and related issues in radiative processes [water vapor is the major greenhouse gas in the atmosphere (Twomey 1991)], and studies of a variety of atmospheric processes such as cloud formation and atmospheric circulation. The Raman lidar is a leading candidate for an instrument capable of the detailed time- and space-resolved measurements required by these and other studies. We describe simultaneous nighttime measurements of water vapor profiles using two collocated Raman lidar systems. We believe that

this is the first detailed intercomparison of chemical species measurements performed using multiple Raman lidar systems, and that the agreement between measurements made using the two independent systems provides a striking example of the capability of the Raman lidar technique.

Raman lidar operates by sending out a laser pulse and recording the atmospherically backscattered return signal as a function of time to provide range information. The return signal consists of an elastically scattered part that is useful for profiling cloud heights, aerosols, and the planetary boundary layer, and inelastically scattered parts that provide chemically specific profiles such as water vapor. The inelastic scattering utilized here is the result of the rotational-vibrational Raman effect that shifts the incident wavelength by a frequency characteristic of the molecule ( $3652 \text{ cm}^{-1}$  for water vapor and  $2331 \text{ cm}^{-1}$  for molecular nitrogen). Simultaneous measurement and subsequent ratioing of the water vapor and nitrogen Raman signals provides a quantitative measurement of the water vapor mixing ratio (grams of water vapor per kilogram of dry air), as first demonstrated by Melfi et al. (1969) and by Cooney (1970). The capabilities of Raman lidar systems have steadily improved by taking advantage of technological advances, particularly those in laser systems (Melfi and Whiteman 1985; Melfi et al. 1989; Ansmann et al. 1992).

Throughout the development of Raman lidar systems, the performance of these systems has normally been assessed by using radiosondes as a "standard" for comparison. Unfortunately, radiosonde packages are by no means ideal standards, showing significant variability among different types of radiosonde humidity sensors at cold temperatures as well as different reporting procedures at low relative humidities (Schmidlin 1989). An additional difficulty is introduced by the fact that balloon-borne packages follow local winds as they ascend; thus, the laser beam and the radiosonde package do not necessarily sample the same portion of the atmosphere.

\*Sandia National Laboratories, Livermore, California.

†Hughes STX Corporation, NASA/Goddard Space Flight Center, Greenbelt, Maryland.

\*\* NASA/Goddard Space Flight Center, Greenbelt, Maryland.

Corresponding author address: J. E. M. Goldsmith, Sandia National Laboratories, Livermore, CA 94551-0969.

In final form 17 December 1993.

© 1994 American Meteorological Society

In this study, we avoid the major limitations inherent in lidar–radiosonde comparisons by directly comparing water vapor profiles measured using two collocated Raman lidar systems. Although radiosonde measurements are required to derive a single calibration constant for each lidar system, all other aspects of this comparison rely only on the lidar measurements and are not limited by the characteristics of other instrumentation in evaluating the performance of the Raman lidars themselves. In particular, this form of comparison provides unambiguous information on the precision (but not absolute accuracy) of Raman lidar systems.

## 2. Raman lidar systems

The Raman lidar systems used in this intercomparison were developed at the NASA/Goddard Space Flight Center and at Sandia National Laboratories (referred to henceforth simply as the Goddard and Sandia lidars). The Goddard lidar is the latest in a series of instruments developed over the past 12 years; the current version was first fielded at the SPECTRE/FIRE campaign in the fall of 1991 (Melfi et al. 1992a; Melfi et al. 1992b), and its performance has been evaluated carefully since that time. The Sandia lidar was constructed during 1992, and the full system

***...we avoid the major limitations inherent in lidar–radiosonde comparisons by directly comparing water vapor profiles measured using two collocated Raman lidar systems.***

became operational in October 1992, just before the intercomparison described here.

The Goddard and Sandia lidars share many characteristics. The systems are housed in two mobile semitrailers each, one trailer serving as a mobile laboratory and the other as a support vehicle providing a data acquisition/analysis area. Both systems employ high average power, high repetition rate excimer lasers as light sources, and have identical telescopes as the primary element of the receiver subsystems. The major differences are in the laser sources and in the design of the optical elements located after the receiving telescope. The Goddard lidar uses an excimer laser configured with unstable resonator optics, operated at 351 nm during the nighttime and at 248 nm during the daytime (solar-blind operation). The system has a single adjustable field of view (FOV) and two complete sets of optics,

one for each operating wavelength. Each set in turn has high- and low-sensitivity channels to provide extended dynamic range for each detection wavelength, with photon counting used in all channels. The Sandia lidar uses an injection-seeded excimer laser to provide a beam with reduced divergence and spectral bandwidth, operated at 308 nm during both nighttime and daytime. The system operates in a dual-FOV configuration for enhanced daytime capabilities. Enhanced dynamic range, for daytime operation in particular, is provided by using photon counting in the narrow FOV channel and analog-to-digital conversion in the wide FOV channel. The characteristics of the systems are summarized in Table 1.

The ratio of the Raman lidar water vapor signal to the nitrogen signal provides a direct relative measurement of water vapor mixing ratio as a function of altitude, requiring only a small correction for differential attenuation at the two return wavelengths (Whiteman et al. 1992). At the beginning of each night, we acquire a separate vertical profile of nitrogen Raman scattering in the water vapor channel by replacing the water vapor interference filter by the nitrogen interference filter. This profile is used for two purposes (Whiteman et al. 1992). By comparing its strength with a profile observed in the nitrogen channel, we obtain a calibration constant that can be maintained from night to night to correct for detector-

channel-specific variations in sensitivity. In addition, the profile is used to correct for small differences in the overlap functions of the water vapor and nitrogen channels for ranges of less than ~1 km, for which the laser beam and the receiver field of view have only partial overlap. This procedure makes it possible to perform quantitative measurements starting very near ground

level. We also note that relative humidity must be derived from the mixing ratio measurement using a collocated temperature profile measured independently (typically by a radiosonde). For this reason, with the exception of one figure, all results will be presented as mixing ratios in units of grams of water vapor per kilogram of dry air.

In order to provide absolute values for the mixing ratio, a single calibration constant must be obtained for the system. One approach for establishing this value is to determine the relative sensitivities of the two channels using radiometric calibration techniques; this approach has been found to provide calibration values with a precision of 12% (Vaughan et al. 1988). A second approach, and the one we use, is to perform critical comparisons of coincident lidar and radiosonde measurements and to determine a single, range-independent scale-factor calibration constant

TABLE 1. Lidar characteristics (showing nighttime configuration of the Goddard system).

Subsystem	Characteristic	Sandia	Goddard
Transmitter	Laser	XeCl Excimer	XeF Excimer
	Wavelength	308 nm (XeCl)	351 nm (XeF)
	Energy/pulse	90 mJ	45 mJ
	Repetition rate	200 Hz	400 Hz
	Bandwidth	3 pm	Three lines*
	Divergence	~0.2 mr	~0.5 mr
Receiver	Configuration	Dall–Kirkham	Dall–Kirkham
	Diameter	0.76 m	0.76 m
	f number	4.5	4.5
	Scanning	Zenith, horizontal only	180° scan, vertical plane
	Channel bandpass	0.4 nm	6–9 nm
	Filter transmission	30%–35%	50%–60%
	Field of view	Dual (0.4 mr, 4 mr)	Adjustable (0.5–3.0 mr)
	Ranges	2 (narrow, wide fov)	2 (low, high sensitivity)
	Channels	3	4
	Species	Rayleigh/aerosol (308 nm) Water vapor (347 nm) Nitrogen (332 nm)	Rayleigh/aerosol (351 nm) Water vapor (403 nm) Nitrogen (383 nm) Oxygen (372 nm)
Electronics	Short range	Analog-to- digital conv.	Photon counting
	Long range	Photon counting	Photon counting
	Range resolution	75 m (0.5 $\mu$ sec)	75 m (0.5 $\mu$ sec)

\*Output contains three lines at 349, 351, and 353 nm (Whiteman et al. 1993).

from the comparison. The “critical” part of the comparison involves taking into account the limitations of both the lidar (primarily decreasing precision with increasing range) and the radiosonde measurements (primarily unreliable response in relatively dry air) in order to obtain the best calibration constant. Repeated comparisons of the Goddard lidar to a variety of radiosonde packages over the past year have demonstrated a short-term (~1 month) reproducibility of  $\pm 3\%$  in the calibration constant, limited largely by the reliability of the radiosonde measurements; the long-term (~1 year) stability of the calibration constant is currently being investigated. For the purposes of this intercomparison, a single calibration constant was determined for each lidar system using lidar–radiosonde comparisons from the four radiosondes launched during the intercomparison, only including radiosonde data below cloud base with relative humidity > 30%.

### 3. Intercomparison configuration and meteorological conditions

This intercomparison was performed at the NASA/Goddard Space Flight Center (GSFC) in Greenbelt, Maryland, the home site of one of the lidar systems. The Sandia lidar was operational at this site from 28 October through 20 November 1992 and was located ~320 m west of, and ~15 m lower in altitude than, the Goddard lidar. Personnel from the NASA Wallops Flight Facility launched radiosondes from a location ~370 m north-east of the Goddard lidar. The lidar systems were operated simultaneously for extended peri-

ods during three nights, with two radiosondes launched during two of the nights to calibrate the lidar systems.

High pressure was located over the region on the two nights (8–9 November and 10–11 November) when radiosondes were launched during lidar operations. This high pressure system was centered over Maryland at 1200 UTC 9 November and gradually moved eastward off the coast by 1200 UTC 11 November. As the ridge drifted eastward, surface wind

***The false-color time–height “images” of the water vapor distribution displayed on the cover of this journal provide a striking illustration of the agreement obtained using the two lidar systems.***

directions shifted from northerly to southwesterly and wind speeds increased. Temperature profiles measured by the radiosondes launched at GSFC as well as those launched by the National Weather Service at Dulles Airport (IAD), Washington, D.C., approximately 50 km west-southwest of GSFC indicated warm advection occurred in the 850–600-mb layer during this two-day time period. The 1000–500-mb layer thickness increased from 5.40 km at 0000 UTC 9 November to 5.58 km at 1200 UTC 11 November. Water vapor also increased during this period. The radiosonde and Raman lidar measurements showed surface water vapor mixing ratios were generally less than  $2.5 \text{ g kg}^{-1}$  (60% relative humidity) during the first night with total precipitable water of approximately 6 mm. As shown on the cover, by 0600 UTC 11 November, the lidars indicated surface water vapor mixing ratios increased above  $6 \text{ g kg}^{-1}$  (60% relative humidity) with total precipitable water of approximately 18 mm.

An increase in cloud cover accompanied the increase in water vapor. No clouds were observed on the night of 8–9 November. As the high pressure ridge moved eastward, however, thin cirrus spread over the area on 10 November. Both lidars showed extensive cirrus clouds at altitudes between 9 and 12 km above GSFC during the night of 10–11 November. Late on 10 November, thin patches of altocumulus were also observed by the lidars. These two cloud types were distinguishable from surface visual observations at the lidar site and from the lidar data. Because both lidar systems also detect scattering by molecules, aerosols, and clouds at the laser wavelength, these two cloud types were identified using these return signals. The cirrus clouds had much higher bases (9–12 km vs 4 km) and much smaller scattered return signals than did the altocumulus clouds.

The false-color time–height “images” of the water vapor distribution displayed on the cover of this journal provide a striking illustration of the agreement obtained using the two lidar systems. Each vertical stripe in the images corresponds to a single profile recorded as a one-minute average with 75-m vertical resolution; thus, each image represents 428 independent vertical profiles. Because clouds attenuate laser beams, it is generally not possible to retrieve water vapor above

cloud base; the altocumulus clouds thus appear in the water vapor mixing ratio images as speckled regions that appear periodically at altitudes above 4 km. With the exception of differences within a few hundred meters from the ground, these images demonstrate the excellent quantitative agreement between

measurements recorded with the two lidar systems. Although not displayed here, equally striking agreement is apparent in the images produced from the datasets recorded on the other two nights during which the lidar systems were operated for extended periods.

The relatively high concentration of water vapor in the lowest kilometer (see cover images) shows the location of the residual mixed layer. This layer was capped by a temperature inversion located at an altitude of 1 km, which persisted throughout the night. Note that both lidar systems show an increase in moisture in this lowest layer suggesting the formation of a shallow nocturnal boundary layer. The dry layer between altitudes of 1 and 2 km was nearly isothermal with a weak inversion located near 2 km. The advection of water vapor and temperature as concentrated between altitudes of 2 and 4 km is shown in the cover figure. A weak inversion, which gradually became weaker after 0000 UTC, was located near the top of this layer at 4 km. The lidar water vapor images show the altocumulus clouds formed near this altitude.

#### **4. Intercomparison results**

Figure 1 displays comparisons of profiles recorded by the lidar systems and the four Vaisala radiosondes used during the intercomparison (launch times indicated on the plots). The lidar profiles represent 10-min averages started at the times that the radiosondes were launched. To provide some feeling for what these measurements represent in terms of relative humidity, we have used the temperature profiles measured by the radiosondes to convert mixing ratio to relative humidity, and we display the 0258 UTC 11

November 1992 profiles expressed as relative humidity in Fig. 2.

The absolute calibration constants of the lidar systems were obtained from these four radiosonde profiles. Although four profiles were used to derive the constants, it should be emphasized that a *single* calibration constant was derived for each lidar system and used to prepare the profiles shown in Fig. 1 and the images displayed on the cover. In general, the lidar profiles show excellent agreement at all altitudes except below about 1 km; the agreement at 0419 UTC on 9 November is not as good, but is nonetheless very reasonable. The differences at low altitudes may be real since the lidar systems were separated by ~320 m and the Sandia system was much nearer the Goddard central heating and refrigeration plant, which often emitted visible plumes of steam. However, the fact that the Sandia measurement approaches 100% relative humidity at ground level (Fig. 2) is an indication that systematic errors in the calibration procedure may be affecting the short-range behavior of the Sandia lidar system, which has not been as extensively studied as the Goddard lidar system.

The statistical uncertainty of the water vapor measurements can be derived directly from the number of photon counts recorded in the water vapor and nitrogen detection channels during the period of the measurement; because the water vapor signal is much weaker than the nitrogen signal, the uncertainty is dominated by the water vapor photon-count rate. Figure 3 displays the uncertainties for the two lidar systems for the 10-min 0258 UTC 11 November 1992 profiles (Fig. 1). Because the Sandia lidar uses analog-to-digital conversion methods at low altitudes, the uncertainty is not as readily determined in this region and is displayed only at altitudes measured by the photon-counting channels (above 2 km). The curve for the Goddard lidar, which uses photon counting in both low- and high-altitude channels, consists of three sections: a section in which measure-

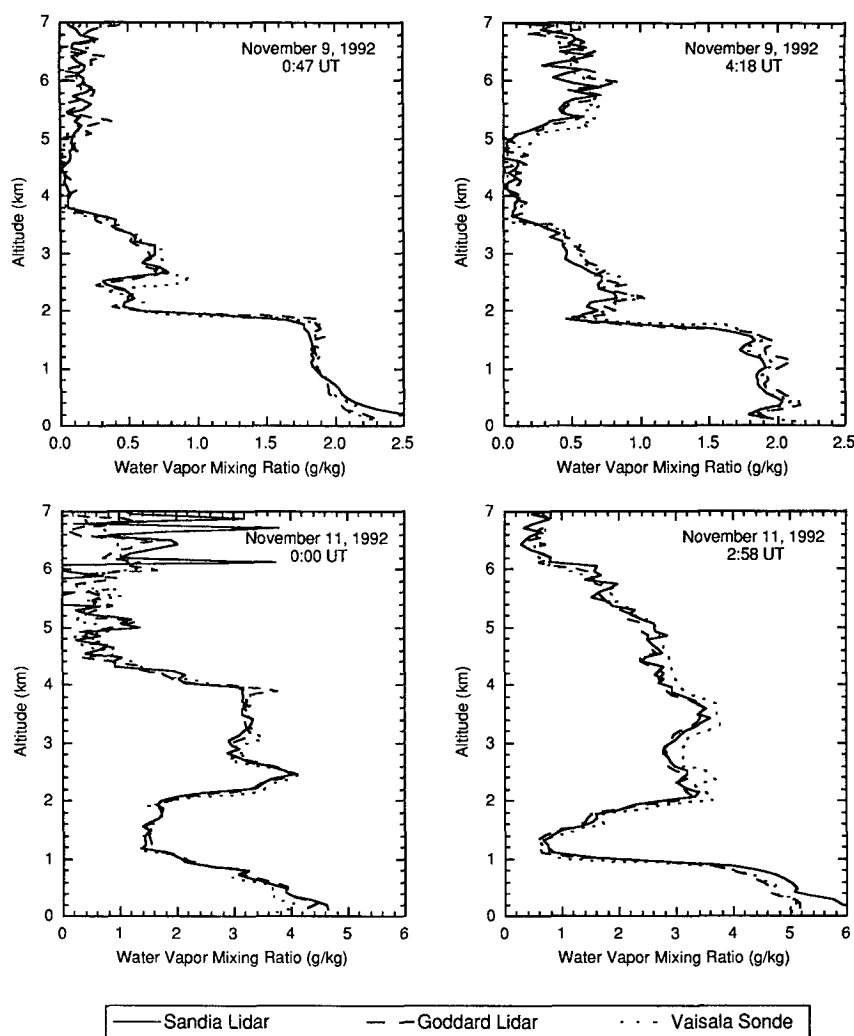


FIG. 1. Water vapor profiles obtained at the indicated times using the Sandia and Goddard Raman lidar systems and Vaisala radiosondes at the NASA/Goddard Space Flight Center (Greenbelt, Maryland). The lidar profiles represent 10-min averages started at the times that the radiosondes were launched.

ments are made only by the low-altitude channel (0–2 km), only by the high-altitude channel (>3 km), and a section in which measurements made by both channels are merged (2–3 km). Shortly after making these measurements, we discovered two problems with the Sandia system that decreased its sensitivity. First, the thyatron reservoir and heater voltages of the laser were misadjusted, causing the laser to seed improperly a significant fraction of the time, increasing the bandwidth and the divergence of the laser. Second, we found that while operating with the field stop chosen to optimize daytime performance of the system (0.4 mrad FOV), approximately half of the signal at altitudes > 2 km was being blocked by the field stop, primarily because the divergence of the laser was significantly larger than had been anticipated. The

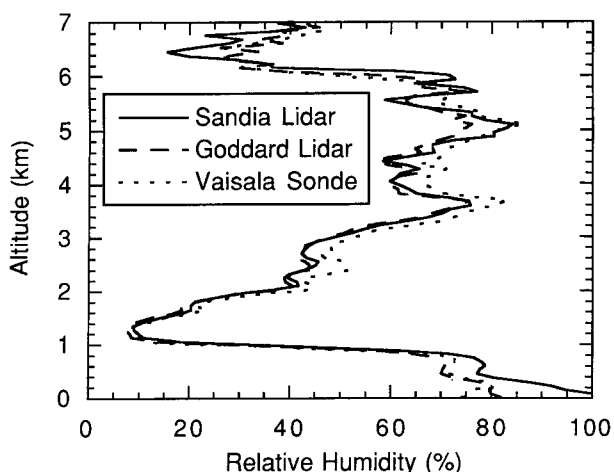


FIG. 2. Relative humidity profiles derived from the 10-min mixing ratio profiles recorded at 0258 UTC on 11 November (Fig. 1) using the radiosonde temperature profile.

statistical uncertainty of measurements made using the Sandia lidar was found to match more closely that of the Goddard lidar after these two problems were corrected.

Raman lidar systems basically measure molecular concentration; thus, their instrumental uncertainty as expressed as absolute humidity (in units of mixing ratio) is relatively insensitive to other meteorological conditions. However, in using the lidar measurements, the percent uncertainty in the water vapor measurement is often of more interest. For the particular conditions represented by Figs. 2 and 3, the uncertainty in the humidity measurements for the Goddard lidar, expressed either as mixing ratio or as relative humidity, increases with altitude slowly from a few percent at 1 km up to 5% at 6 km, and then increases to a larger uncertainty of 20%–30% in the range 6–7 km because of the abrupt drying of the atmosphere above 6 km. For the configuration used in these measurements, the relative uncertainty of measurements made with the Sandia lidar was approximately double the uncertainty of that for the Goddard lidar for the reasons described in the previous paragraph. Because the relative uncertainty depends not only on the lidar characteristics, but also on the humidity of the air being observed, which can vary tremendously, values of percent uncertainty derived for a single measurement should not be considered as representative.

The differences between the water vapor mixing ratio profiles acquired at the times of the four radiosonde launches were examined as a function of altitude. Bias and root-mean-square (rms) differences among the three sensors averaged over the four times were compared and are shown in Figs. 4 and 5,

respectively. The lidar data used for these comparisons were 10-min averages with 75-m vertical resolution. Since all three sensors measured water vapor at slightly different altitudes, the data were linearly interpolated to the same 75-m altitude spacing. To reduce the statistical noise, the differences were averaged over 1-km altitude bins. These figures generally show excellent agreement among the sensors for altitudes between about 1 and 5 km. Below 1 km the rms water vapor mixing ratio differences between the Sandia lidar and the other two sensors increased from about 0.1 to nearly 0.3 g kg<sup>-1</sup>. These differences are a combination of both atmospheric and instrumental effects. Above 6 km the differences among the measurements increases rapidly as the noise associated with the lidar measurements increases. Increasing the averaging times or decreasing the vertical resolution or both reduces the noise and the differences among the instruments.

Recent interest in the effects of water vapor on atmospheric radiative transfer has led us to examine the ability of Raman lidar systems to measure water vapor in the upper troposphere. Several key instrumental (laser power and wavelength, averaging time, vertical resolution, photomultiplier noise) and environmental factors (ambient water vapor concentration, background skylight, atmospheric molecular and aerosol attenuation) that impact this ability have been studied using simulations of and actual data from the GSFC system. By increasing the averaging time from one to two hours, and by degrading the vertical resolution from 75 to 300 m, water vapor retrievals from the GSFC system have been obtained to approximately 9.5 km (~300 mb) with an estimated precision of 5%–

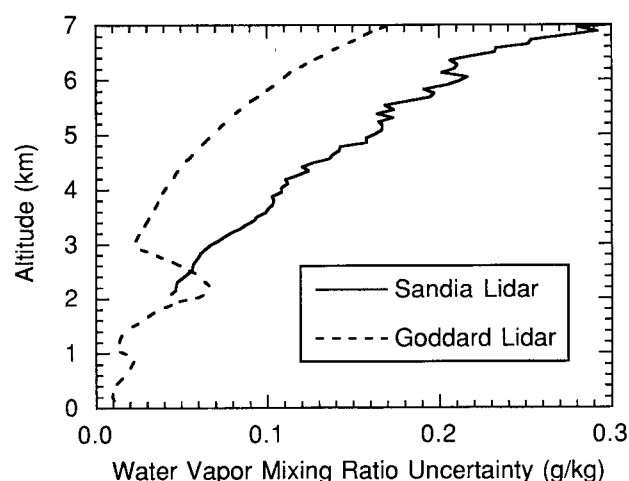


FIG. 3. Statistical uncertainties of the lidar water vapor measurements for the 10-min profiles recorded at 0258 UTC on 11 November (Fig. 1).

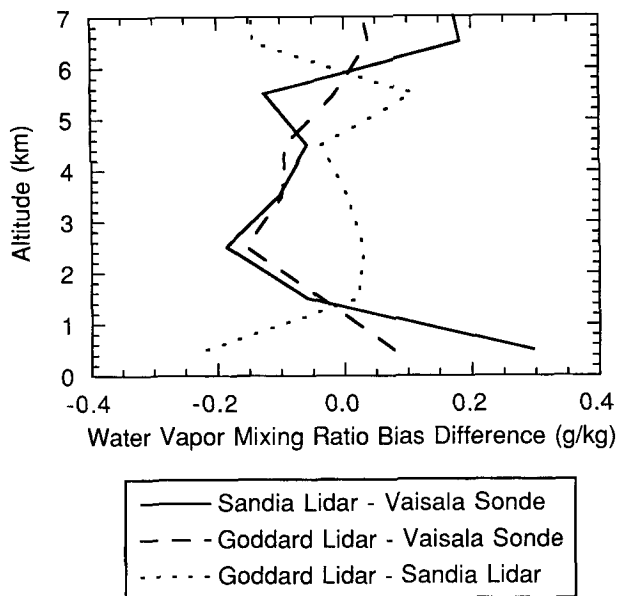


FIG. 4. Bias differences in the water vapor mixing ratios averaged over the four measurements shown in Fig. 1.

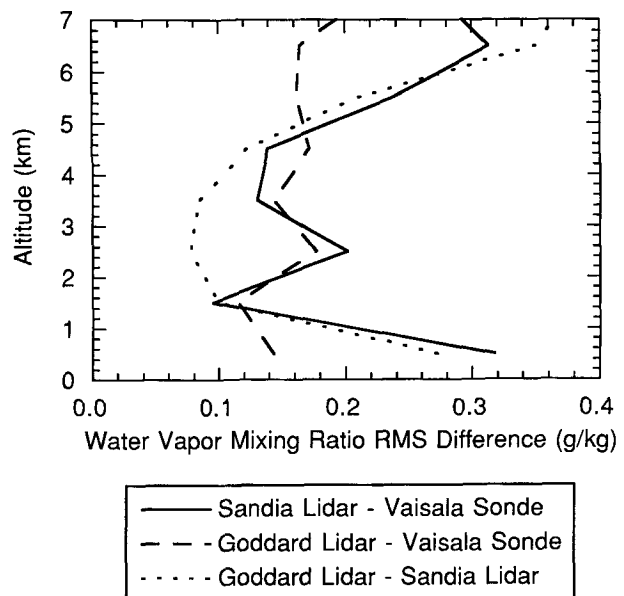


FIG. 5. Root-mean-square differences in the water vapor mixing ratios averaged over the four measurements shown in Fig. 1.

7% (Soden et al. 1993). Computer modeling has shown that this maximum altitude can vary between 8.5 and 10 km depending primarily on the background skylight, ambient water vapor concentration, and aerosol attenuation. It is worth emphasizing that the temporal and spatial bins chosen for recording the data represent the maximum resolutions that are obtained, but that it is straightforward to trade off reduced spatial or temporal resolution or both to obtain improved statistical uncertainty in this manner *at any time* during postacquisition data processing.

## 5. Summary and conclusions

We believe that this intercomparison provides a clear example of the quantitative capabilities of the Raman lidar technique for profiling atmospheric water vapor. Previous intercomparisons have used radiosondes to assess the performance of such lidar systems. The poor temporal frequency of radiosondes, differences in the atmospheric volumes sampled by lidar and radiosondes, and variabilities within various radiosonde packages have limited their usefulness in assessing the performance of Raman lidar. By comparing the high temporal and spatial resolution water vapor profiles measured by two collocated Raman lidar systems, many of the aforementioned limitations were avoided. This intercomparison found rms differences between water vapor mixing ratio profiles of less than  $0.15 \text{ g kg}^{-1}$  for measurements performed by

two lidar systems having substantial differences in their instrumental characteristics, in particular in their excitation wavelengths and the designs of their detector packages. Larger differences in water vapor mixing ratio profiles occurred in the lowest kilometer because of atmospheric and instrumental effects.

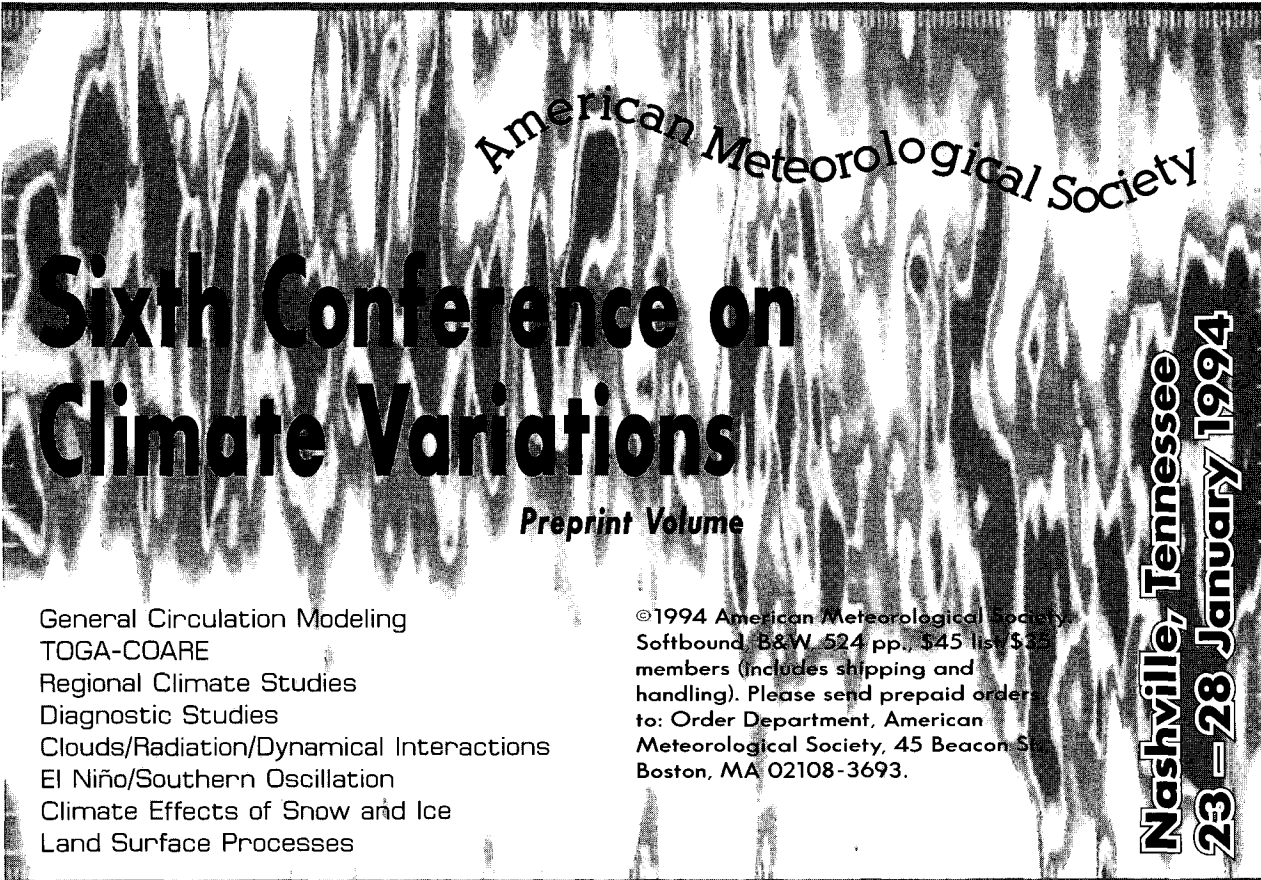
Because quantitative operation of Raman lidars has been most thoroughly developed for nighttime operation, this intercomparison was performed at nighttime, but we are also enhancing the daytime capabilities of these systems (Bisson and Goldsmith 1993; Whiteman et al. 1993), and we hope to perform a daytime intercomparison in the future. Finally, Raman lidar systems also provide quantitative profiles of temperature (Evans et al. 1993) and aerosol properties (Ferrare et al. 1992), suggesting future intercomparisons of these atmospheric characteristics as well.

*Acknowledgments.* We wish to thank Marshall Lapp and John Vitko for many helpful discussions, Mark Mitchell and Glenn Staley for their expert technical assistance, and Prentice Moore and Sam West for providing radiosonde support at the lidar site. This work is supported by the U.S. Department of Energy, Atmospheric Radiation Measurement (ARM) program, and by the NASA Atmospheric Dynamics and Radiation Program.

## References

- Ansmann, A., M. Riebesell, U. Wandinger, C. Weitkamp, E. Voss, W. Lahmann, and W. Michaelis, 1992: Combined Raman elas-

- tic-backscatter lidar for vertical profiling of moisture, aerosol extinction, backscatter, and lidar ratio. *Appl. Phys. B*, **55**, 18–28.
- Bisson, S. E., and J. E. M. Goldsmith, 1993: Daytime tropospheric water vapor profile measurements with a Raman lidar. *Optical Remote Sensing of the Atmosphere Technical Digest*, 1993, Optical Society of America, 19–22.
- Cooney, J., 1970: Remote measurements of atmospheric water vapor profiles using the Raman component of laser backscatter. *J. Appl. Meteor.*, **9**, 182–184.
- Evans, K. D., R. A. Ferrare, S. H. Melfi, and D. N. Whiteman, 1993: Tropospheric temperature measurements using a Raman lidar. *Optical Remote Sensing of the Atmosphere Technical Digest*, 1993, Optical Society of America, 169–172.
- Ferrare, R. A., S. H. Melfi, D. N. Whiteman, and K. D. Evans, 1992: Raman lidar measurements of Pinatubo aerosols over southeastern Kansas during November–December 1991. *16th Int. Laser Radar Conf.*, NASA Conference Publication 3158, 13–16.
- Melfi, S. H., and D. N. Whiteman, 1985: Observation of lower-atmospheric moisture structure and its evolution using a Raman lidar. *Bull. Amer. Meteor. Soc.*, **66**, 1288–1292.
- , J. D. Lawrence Jr., and M. P. McCormick, 1969: Observation of Raman scattering by water vapor in the atmosphere. *Appl. Phys. Lett.*, **15**, 295–297.
- , D. Whiteman, and R. Ferrare, 1989: Observation of atmospheric fronts using Raman lidar moisture measurements. *J. Appl. Meteor.*, **28**, 789–806.
- , —, —, S. E. Bisson, J. E. M. Goldsmith, and M. Lapp, 1992a: Atmospheric water vapor measurements during the SPECTRE campaign using an advanced Raman lidar. *Conference on Lasers and Electro-Optics*, 1992, OSA Technical Digest Series, Vol. 12, Optical Society of America, 428–429.
- , —, —, K. Evans, J. E. M. Goldsmith, M. Lapp, and S. E. Bisson, 1992b: Raman lidar measurements of water vapor and aerosol/clouds during the FIRE/SPECTRE Field Campaign. *16th Int. Laser Radar Conf.*, NASA Conference Publication 3158, 663–666.
- Schmidlin, F. J., 1989: WMO international radiosonde comparison, phase II final report, 1985. *Instruments and Observing Methods Report*, No. 29 WMO/TD-No. 312, WMO.
- Soden, B. J., S. A. Ackerman, D. O'C. Starr, S. H. Melfi, and R. A. Ferrare, 1993: Comparison of upper tropospheric water vapor from GOES, Raman lidar, and CLASS measurements during FIRE Cirrus-II. *J. Geophys. Res.*, submitted.
- Twomey, S., 1991: Aerosols, clouds, and radiation. *Atmos. Environ.*, **25A**, 2435–2442.
- Vaughan, G., D. P. Wareing, L. Thomas, and V. Mitev, 1988: Humidity measurements in the free troposphere using Raman backscatter. *Quart. J. Roy. Meteor. Soc.*, **114**, 1471–1484.
- Whiteman, D. N., S. H. Melfi, and R. A. Ferrare, 1992: Raman lidar system for the measurement of water vapor and aerosols in the Earth's atmosphere. *Appl. Opt.*, **31**, 3068–3082.
- , —, —, and K. D. Evans, 1993: Solar blind Raman scattering measurements of water vapor using a KrF excimer laser. *Optical Remote Sensing of the Atmosphere Technical Digest*, 1993, Optical Society of America, 165–168.
- , W. F. Murphy, N. W. Walsh, and K. D. Evans, 1993: Temperature sensitivity of an atmospheric Raman lidar system based on a XeF excimer laser. *Opt. Lett.*, **18**, 247–249.



**American Meteorological Society**

# Sixth Conference on Climate Variations

**Preprint Volume**

General Circulation Modeling  
TOGA-COARE  
Regional Climate Studies  
Diagnostic Studies  
Clouds/Radiation/Dynamical Interactions  
El Niño/Southern Oscillation  
Climate Effects of Snow and Ice  
Land Surface Processes

©1994 American Meteorological Society  
Softbound, B&W, 524 pp., \$45 list \$25  
members (includes shipping and  
handling). Please send prepaid order  
to: Order Department, American  
Meteorological Society, 45 Beacon St.,  
Boston, MA 02108-3693.

**Nashville, Tennessee**  
**23–28 January 1994**